RETINEX BASED ON EXPONENT-TYPE TOTAL VARIATION SCHEME

Lu Liu

Center for Applied Mathematics
Tianjin University, Tianjin, P.R. China

Zhi-Feng Pang

School of Mathematics and Statistics, and Laboratory of Data Analysis Technology
Henan University, Kaifeng, 475004, P.R. China

Yuping Duan*

Center for Applied Mathematics
Tianjin University, Tianjin, P.R. China

(Communicated by the associate editor name)

Abstract. Retinex theory deals with compensation for illumination effects in images, which has a number of applications including Retinex illusion, medical image intensity inhomogeneity and color image shadow effect etc.. Such ill-posed problem has been studied by researchers for decades. However, most exiting methods paid little attention to the noises contained in the images and lost effectiveness when the noises increase. The main aim of this paper is to present a general Retinex model to effectively and robustly restore images degenerated by both illusion and noises. We propose a novel variational model by incorporating appropriate regularization technique for the reflectance component and illumination component accordingly. Although the proposed model is non-convex, we prove the existence of the minimizers theoretically. Furthermore, we design a fast and efficient alternating minimization algorithm for the proposed model, where all subproblems have the closed-form solutions. Applications of the algorithm to various gray images and color images with noises of different distributions yield promising results.

1. **Introduction.** Decomposition an image into meaningful components is the real substance of many tasks in image processing, such as image denoising, which decomposes the image into signal parts and noise parts [1, 2]; image structure-texture decomposition, where images are modeled as a combination of geometrical information and textural information [3, 4]. Retinex [5] is a related but different topic,

2010 *Mathematics Subject Classification.* 80M30, 80M50, 68U10.

Key words and phrases. Retinex, Image decomposition, Image restoration, High-order model, Alternating minimization algorithm.

The work is supported by the 1000 Talents Program for Young Scientists of China, the Ministry of Science and Technology of China ("863" Program: 2015AA020101), and NSFC 11701418 and 11526208. Dr. Z.-F. Pang was partially supported by National Basic Research Program of China (973 Program No.2015CB856003) and NSFC (Nos.U1304610 and 11401170), and also gratefully acknowledges financial support from China Scholarship Council(CSC) as a research scholar to visit the University of Liverpool from August 2017 to August 2018.

* Corresponding author: Yuping Duan. yuping.duan@tju.edu.cn.

which was originally proposed by Land and McCann [5] as a model of color perception of the human visual system. It reveals that human vision tends to see the same color in a given image regardless the light and the color of objects remains relatively constant under varying illumination. Thus, the goal of Retinex is to decompose the illumination from the reflectance in given images. In fact, such problem also exists in medical image processing, the so-called intensity inhomogeneity, which leads to the intensity variation even for the same tissue within an image. The importance of Retinex is that it can facilitate other image analysis techniques such as segmentation, registration, etc., that relying on the assumption of uniform intensity.

To set up the Retinex problem mathematically, we focus on decomposing a given image I into the reflectance component R and the illumination component L as

$$I(x,y) = R(x,y) \cdot L(x,y), \tag{1}$$

The following general assumptions exists as the basic laws for Retinex:

- The reflectance $R(x,y)$ is a piecewise constant function;
- The illumination $L(x,y)$ is a spatial smooth function.

Since the logarithmic transform can preserve image edges and simplify the relationship between R and L, most Retinex algorithms are proposed in the logarithmic domain, which gives

$$i(x,y) = r(x,y) + l(x,y), \tag{2}$$

where $i = \log(I)$, $l = \log(L)$, $r = \log(R)$.

Various implementations and algorithms have been studied for Retinex problem. Path-based methods were originated by Land and McCann [5, 6], and further studied in [7, 8]. Recursive algorithms were proposed by using a recursive matrix calculation to replace the path computation in [9, 10]. Homomorphic filtering type Retinex algorithms modeled the reflectance as a low-pass version of the given image based on a convolution with a wide Gaussian kernel [11, 12]. Bertalmío *et al.* [13] proposed a kernel-based Retinex algorithm relying on the computation of the expectation value of a suitable random variable weighted with a kernel function. Retinex was also considered in an alternative perspective [14, 15], the so-called color correction, both of which were built up in the variational framework.

In PDE-based models and variational formulations, Morel *et al.* [16] formulated the illumination as a spatially smooth image and the reflectance as a piecewise constant image, which was solved as a Poisson equation by Fast Fourier Transform (FFT). Based on the assumption of the spatial smoothness of the illumination, Kimmel *et al.* [17] proposed a variational model by penalizing on the reflectance. Elad [18] proposed a noniterative Retinex algorithm by utilizing two bilateral filters as the regularization term. Ng and Wang [19] proposed a similar model by penalizing both the reflectance and illumination images. Ma and Osher [20] developed a Total Variation (TV) [1] based model to extract the reflectance image with a data term in gradient field. Zosso *et al.* [21] further extended the TV-based Retinex models to a unified non-local formulation. Chang *et al.* [22] proposed a variational model for Retinex by representing the reflectance component with more details by a learned dictionary. Duan *et al.* [23, 24] investigated variational models for Retinex using ℓ^0 quasi-norm to regularize the reflectance image. Liang and Zhang [25] proposed a convex Retinex model, which decompose the gradient field of images into salient edges and relatively smoother illumination field.

Various algorithms have gained great success in dealing with Retinex problems. However, these methods paid little attention to the noises contained in given images, as they are all based on the image model (1), which does not model noises as a component. Especially, when the logarithmic transform is taken as (2), the distribution of the noises becomes more complicated, and even harder to remove. In fact, illusion (intensity inhomogeneity) and noises may simultaneously exist in given images, such as MR images, ultrasound images etc.. Therefore, when the observed images are corrupted by noises, these methods lost their effectiveness in recovering the reflectance image with high quality.

1.1. **Our contributions.** In this paper, we propose a general variational model for images in presence of both illusion and noises, that is we consider the following image model

$$I(x,y) = (R(x,y) \cdot L(x,y)) \oplus n(x,y). \tag{3}$$

The multiplicative relation between R and L can be transformed into the addition one as follows

$$I(x,y) = V(x,y) \oplus n(x,y), \quad \text{s.t., } v(x,y) = r(x,y) + l(x,y), \tag{4}$$

where $v = \log V$, $\oplus$ represents the effect of noises, which indicates $+$ for additive noise and $\times$ for multiplicative noise. Based on (4), we reported in [26] the idea of recovering the noise-free image V from the given image I, and decomposing it into the reflectance r and illumination l in the logarithmic domain. However, only preliminary results were presented and some advantages were observed, where we extend the idea in both theoretically and numerically in this work. To be specific, we use total variation as the regularization for V and choose the date fidelity according to the distribution of the noise model. For the decomposition, the first- and second-order TV regularization are implemented as [25]. Furthermore, we propose an efficient alternating minimization (AM) algorithm, all subproblems of which can be efficiently solved by the closed-form solutions. Numerous experiments on synthetic and real images demonstrate that our model gives better results in comparison with other state-of-the-art Retinex methods, especially when noises is significant. In addition, three main contributions are presented:

1. We propose a variational model to recover images corrupted by illusion and noises, which is guaranteed with the existence of minimizers.
2. Our proposed model is capable to deal with different types of noises, such as Gaussian noise, impulsive noise [27] and Poisson noise [28] etc., as long as we modify the data fidelity term according to the noise distribution.
3. Our framework can be easily extended to other Retinex models, such as Ng and Wang's Retinex model [19], ℓ^0 regularized Mumford-Shah model [23, 24], etc..

The rest of the paper is organized as follows. In Section 2, we introduce the notations that will be used in the rest of the paper. We briefly review the variational models for Retinex. In Section 3, we propose our new model for recovering images corrupted by illusion and noises. Furthermore, the existence of the solution to the proposed model is provided and the proofs of the mathematical results are shown. In section 4, we design an alternating minimization algorithm for the proposed model and discuss the solutions to each sub-minimization problem. In Section 5, we present the numerical experiments on both synthetic medical images, visual

illusion images and real medical images, color images. We then conclude the paper in Section 6 with some final remarks and future prospects.

2. Setting and previous works.

2.1. Discretization.

Without loss of generality, we present a grayscale image as a two dimension matrix of size $N \times N$, the size of matrix here can also be $M \times N$. We denote X the Euclidean space $\mathbb{R}^{N\times N}$, which is equipped with the usual inner product and Euclidean norm as $\langle\cdot,\cdot\rangle$ and $\|\cdot\|_2$, respectively. The discrete gradient operator is a mapping $\nabla : X \to Y$, where $Y = X \times X$. For $u \in X$, ∇u is given by

$$(\nabla u)_{j,k} = \big((\mathring{D}_x^+ u)_{j,k}, (\mathring{D}_y^+ u)_{j,k}\big),$$

with

$$(\mathring{D}_x^+ u)_{j,k} = \begin{cases} u_{j,k+1} - u_{j,k}, & 1 \le k \le N-1, \\ u_{j,1} - u_{j,N}, & k = N, \end{cases}$$

$$(\mathring{D}_y^+ u)_{j,k} = \begin{cases} u_{j+1,k} - u_{j,k}, & 1 \le j \le N-1, \\ u_{1,k} - u_{N,k}, & j = N, \end{cases}$$

where $j, k = 1, \ldots, N$. Here we use $\mathring{D}_x^+$ and $\mathring{D}_y^+$ to denote forward difference operators with the periodic boundary conditions.

We also equip the space Y with the inner product $\langle \boldsymbol{p}, \boldsymbol{q}\rangle = \langle p^1, q^1\rangle + \langle p^2, q^2\rangle$ and the norm $\|\boldsymbol{p}\|_1 = \sum_{1\le i,j\le N} \sqrt{(p_{i,j}^1)^2 + (p_{i,j}^2)^2}$, and $\|\boldsymbol{p}\|_2 = \sqrt{\langle \boldsymbol{p}, \boldsymbol{p}\rangle}$. The discrete divergence operator $\mathrm{div} = -\nabla^*$ is a mapping $Y \to X$, where ∇^* is the adjoint of ∇. Given $\boldsymbol{p} \in Y$, we have

$$(\mathrm{div}\boldsymbol{p})_{j,k} = (\mathring{D}_x^- p^1)_{j,k} + (\mathring{D}_y^- p^2)_{j,k}$$

with

$$(\mathring{D}_x^- p^1)_{j,k} = \begin{cases} p_{j,k}^1 - p_{j,k-1}^1, & 2 \le k \le N, \\ p_{j,1}^1 - p_{j,N}^1, & k = 1, \end{cases}$$

$$(\mathring{D}_y^- p^2)_{j,k} = \begin{cases} p_{j,k}^2 - p_{j-1,k}^2, & 2 \le j \le N, \\ p_{1,k}^2 - p_{N,k}^2, & j = 1, \end{cases}$$

where $\mathring{D}_x^-$ and $\mathring{D}_y^-$ to denote backward difference operators with the periodic boundary conditions.

2.2. TVH1 model.

We review some important variational models for Retinex. Kimmel *et al.* [17] proposed a variational Retinex model as follows

$$\min_r \ \frac{1}{2}\|r - i\|_2^2 + \alpha\|\nabla r\|_1 + \frac{\beta}{2}\|\nabla(r - i)\|_2^2, \tag{5}$$

where α and β are positive constants. The first term in (5) is used for the fidelity, while the reflectance part and the illumination part are regularized by the TV norm and H^1 norm, respectively.

Ng and Wang further studied the total variation model for Retinex in [19], where they explicitly minimized both r and l in the energy functional with box constraints

$$\min_{r\le 0, l\ge i} \ \frac{1}{2}\|l - r - i\|_2^2 + \alpha\|\nabla r\|_1 + \frac{\beta}{2}\|\nabla l\|_2^2 + \frac{\tau}{2}\|l\|_2^2, \tag{6}$$

where τ is a positive constant, and the constraint $l \ge i$ is given based on the assumption that R is the reflectivity and $0 < R \le 1$.

2.3. **HoTVL1 model.** Recently, Liang and Zhang [25] presented a high order TV based model for reflectance and illumination decomposition, which reads

$$\min_{r\in\mathcal{B}_r, l\in\mathcal{B}_l} \frac{1}{2}\|i-r-l\|_2^2+\alpha\big(\|\nabla r\|_1+\beta\|\nabla^2 l\|_1\big)+\frac{\tau}{2}\|l\|_2^2, \tag{7}$$

where the first- and second-order TV are introduced to regularize the reflectance and illumination, respectively. The box constraints are imposed on both r and l, which vary with different applications.

2.4. **L0MS model.** Duan et al. [24] built up an unconstrained variational model based on the Mumford-Shah formulation for images with intensity inhomogeneity as follows

$$\min_{r,l} \frac{1}{2}\mathcal{E}(r,l)+\alpha\|\nabla r\|_0+\frac{\beta}{2}\|\nabla l\|_2^2+\frac{\tau}{2}\|l\|_2^2, \tag{8}$$

where $\mathcal{E}(r,l)=\sum_{p\in\Omega}\big(\sum_{q\in\mathcal{N}_p} K(x_p-x_q)(i_q-r_q-l_p)^2\big)$, and for a given pixel $p\in\Omega$, $\mathcal{N}_p=\{q|\ |p-q|\le\rho\}$ is its neighborhood with a radius ρ. In (8), r and l are regularized by the ℓ^0 quasi-norm and the H^1 norm, respectively. Unlike other methods, L0MS model gives an exact piecewise constant solution of r, which is a preliminary results for structural segmentation. Thus, the ℓ^0 regularized Retinex model has been reformulated for three-dimensional applications based on the high-order regularization in [29].

3. Problem formulation.

3.1. **The proposed model.** In real applications, the observed images are usually contaminated by both illusion and noises. Consequently, we aim to recover the noise-free image, and decompose it into reflectance image and illumination image. More specifically, we propose a novel Retinex model by combining the HoTVL1 model (7) and a data fidelity term deriving from the noise models. We use the additive Gaussian noise as an example, and propose the following unconstrained minimization problem

$$\min_{v,r,l} \mathcal{F}(v,r,l):=\frac{1}{2}\|I-e^v\|_2^2+\alpha\|\nabla e^v\|_1+\beta\|\nabla r\|_1+\gamma\|\nabla^2 l\|_1+\frac{\mu}{2}\|v-r-l\|_2^2+\frac{\tau}{2}\|l\|_2^2, \tag{9}$$

where $V=e^v$ according to the image model (4). The main advantage of using the exponential function other than the logarithmic function is its convexity [30]. Obviously, the above model can be easily adapted to other noise models by choosing an appropriate data fidelity term, which will be discussed in the section of numerical experiments.

3.2. **Existence of solution.** Although the energy functional $\mathcal{F}(v,r,l)$ in (9) is non-convex, we are still able to show the existence of its minimizers. On the first place, we prove that the objective function $\mathcal{F}(v,r,l)$ is coercive as follows.

Lemma 3.1. *Assume that $Ker(\nabla)\cap Ker(\nabla^2)=\{0\}$, the functional $\mathcal{F}(v,r,l)$ defined in (9) is coercive.*

Proof. The proof is motivated by Lemma 3.8 in [30]. The lower bound of the discrete TV is given by

$$\|\nabla r\|_1=\sum_{1\le j,k\le N}\sqrt{\big(r_x(j,k)\big)^2+\big(r_y(j,k)\big)^2}\ge\frac{1}{\sqrt{2}}\|\boldsymbol{L}r\|_1,$$

where $\boldsymbol{L}$ is the first-order difference matrix defined by the one-sided difference matrix on the horizontal direction D_x and the vertical direction D_y as

$$\boldsymbol{L} = \begin{pmatrix} D_x \\ D_y \end{pmatrix}.$$

The null space of $\boldsymbol{L}$ is the set $\{c_1\mathbf{1}\}$ with c_1 being a scalar. On the other hand, the lower bound of the discrete high-order TV is given as

$$\begin{aligned}\|\nabla^2 l\|_1 &= \sum_{1\le j,k\le N} \sqrt{\big(l_{xx}(j,k)\big)^2 + \big(l_{xy}(j,k)\big)^2 + \big(l_{yx}(j,k)\big)^2 + +\big(l_{yy}(j,k)\big)^2} \\ &\ge \frac{1}{2}\sum_{1\le j,k\le N} |l_{xx}(j,k)| + |l_{xy}(j,k)| + |l_{yx}(j,k)| + |l_{yy}(j,k)| = \frac{1}{2}\|\boldsymbol{H} l\|_1,\end{aligned}$$

where $\boldsymbol{H}$ is defined as

$$\boldsymbol{H} = \begin{pmatrix} D_{xx} \\ D_{xy} \\ D_{yx} \\ D_{yy} \end{pmatrix},$$

with D_{xx}, D_{xy}, D_{yx} and D_{yy} being the second-order difference matrixes. The null space of $\boldsymbol{H}$ is the set $\{c_2\mathbf{1}\}$ with c_2 being a scalar.

Let $\mathcal{F}_1(v,r,l) = \|v-r-l\|_2^2$ and $\mathcal{F}_2(r,l) = \beta\|\boldsymbol{L}r\|_1 + \gamma\|\boldsymbol{H}l\|_1$. Based on the assumption that $Ker(\nabla)\cap Ker(\nabla^2) = \{0\}$, we can denote

$$\Gamma = \big\{(v,r,l) \mid \frac{\mu}{2}\mathcal{F}_1(v,r,l) + \mathcal{F}_2(r,l) = 0\big\}.$$

We consider two cases: (i) $(v,r,l)\notin\Gamma$ with $\|(v,r,l)\|_2\to\infty$ [1] and (ii) $(v,r,l)\in\Gamma$ with $\|(v,r,l)\|_2\to\infty$, respectively.

For case (i), consider $(v,r,l)\notin\Gamma$ with $\|(v,r,l)\|_2\to\infty$, we can discuss according to the value of v, r and l and easily obtain

$$\mathcal{F}(v,r,l) \ge \frac{1}{2}\|I-e^v\|_2^2 + \frac{\mu}{2}\mathcal{F}_1(v,r,l) + \mathcal{F}_2(r,l) + \frac{\tau}{2}\|l\|_2^2 \to \infty.$$

For case (ii), consider $(v,r,l)\in\Gamma$, there is $v = r+l$, $r = c_1\mathbf{1}$, and $l = c_2\mathbf{1}$. Since $\|(v,r,l)\|_2\to\infty$, i.e., at least $|c_1|\to\infty$ or $|c_2|\to\infty$,we have

$$\mathcal{F}(v,r,l) \ge \frac{1}{2}\|I-e^v\|_2^2 + \frac{\tau}{2}\|l\|_2^2 \to \infty.$$

□

In order to establish the existence of the minimizers for (9), we first present some preliminaries for the bounded Hessian (BH) space. Let Ω be an open subset of $\mathbb{R}^{N\times N}$ with Lipschitz boundary. Then we set $\mathrm{BV}(\Omega) = \{u \mid |u|_{TV} < \infty\}$, where $|u|_{TV} = \sum|Du|$. We consider v, r in the bounded variation space $\mathrm{BV}(\Omega)$ and l in the bounded Hessian space $\mathrm{BH}(\Omega)$, where $\mathrm{BH}(\Omega) = \{l \mid \|D^2 l\|_1 < \infty\}$. We extend some main properties of the high-order total variation space in [25, 31] to the following forms of the discretized space $\mathrm{BH}(\Omega)$.

- Suppose that $\{u^k\}_{k\in\mathbb{N}}$ is bounded in $\mathrm{BH}(\Omega)$, then there exists a subsequence $\{u^{k_j}\}_{j\in\mathbb{N}}$ and $u\in\mathrm{BH}(\Omega)$ such that $\{u^{k_j}\}_{j\in\mathbb{N}}$ weakly* converges to u.

[1] $\|(\cdot,\cdot,\cdot)\|_2$ is the usual ℓ^2 norm defined as $\|(v,r,l)\|_2 = \sqrt{v^2+r^2+l^2}$.

- If Ω has a Lipschitz boundary and it is connected, then it can be shown that there exists positive constants C_1, C_2 such that

$$\|\nabla u\|_1 \leq C_1\|D^2u\|_1 + C_2\|u\|_1. \tag{10}$$

Theorem 3.2. *The problem (9) has at least one solution* $(v^*, r^*, l^*) \in \mathrm{BV}(\Omega) \times \mathrm{BV}(\Omega) \times \mathrm{BH}(\Omega)$.

Proof. Let us pick a minimizing sequence $(v^n, r^n, l^n) \in \mathrm{BV}(\Omega) \times \mathrm{BV}(\Omega) \times \mathrm{BH}(\Omega)$. Since $\mathcal{F}$ is coercive, (v^n, r^n, l^n) must be bounded. So we have $\mathcal{F}(v^n, r^n, l^n) \to \inf \mathcal{F}(v, r, l)$ as $n \to \infty$. Then, there exists a constant $M > 0$ such that $\mathcal{F}(v^n, r^n, l^n) \leq M$. Thus each term in $\mathcal{F}(v^n, r^n, l^n)$ is bounded, i.e.,

$$\|\nabla r^n\|_1 \leq M,\ \|l^n\|_2^2 \leq M,\ \|\nabla^2 l^n\|_1 \leq M,$$
$$\|\nabla e^{v^n}\|_1 \leq M,\ \|I - e^{v^n}\|_2^2 \leq M,\ \|v^n - r^n - l^n\|_2^2 \leq M.$$

First, since $r^n \in [A, 0], \|r^n\|_1 = \int_\Omega |r^n| dx \leq |A||\Omega|$, where $A = \min \log(I), I \in (0, 1]$ and $|\Omega|$ is the area of Ω. Hence, $\|r^n\|_{\mathrm{BV}(\Omega)}$ is uniformly bounded. By the compactness property of $\mathrm{BV}(\Omega)$ and the relative compactness of $\mathrm{BV}(\Omega)$ in $\ell^1(\Omega)$, up to a subsequence also denoted by $\{r^n\}$ after relabeling, there exists a function $r^* \in \mathrm{BV}(\Omega)$ such that (a) $r^n \to r^*$ strongly in $\ell^1(\Omega)$, (b) $r^n \to r^*$ a.e. $x \in \Omega$, (c) $\nabla r^n \rightharpoonup \nabla r^*$ in the sense of measure. The lower semi-continuity of the total variation leads to

$$\|\nabla r^*\|_1 \leq \liminf_{n\to\infty} \|\nabla r^n\|_1. \tag{11}$$

Similarly, we can derive that $\{l^n\}$ is bounded in $\ell^1(\Omega)$. By virtue of the embedding inequality (10), we also have

$$\|\nabla l^n\|_1 < C_1\|D^2 l^n\|_1 + C_2\|l^n\|_1 < M',$$

where M' is a constant number for all $n \in \mathbb{N}$. Thus $\{l^n\}$ is uniformly bounded in $\mathrm{BH}(\Omega)$, up to a subsequence also denoted by $\{l^n\}$ after relabeling, there exists a function $l^* \in \mathrm{BH}(\Omega)$ such that (a) $l^n \to l^*$ strongly in $\ell^1(\Omega)$, (b) $l^n \to l^*$ a.e. $x \in \Omega$, (c) $\nabla^2 l^n \rightharpoonup \nabla^2 l^*$ weakly in $\mathrm{BH}(\Omega)$. The lower semi-continuity of ℓ^2-norm and ℓ^1-norm leads to

$$\begin{aligned} \|l^*\|_2^2 &\leq \liminf_{n\to\infty} \|l^n\|_2^2; \\ \|\nabla^2 l^*\|_1 &\leq \liminf_{n\to\infty} \|\nabla^2 l^n\|_1. \end{aligned} \tag{12}$$

Next, similarly since $v^n \in [A, 0], \|v^n\|_1 = \int_\Omega |v^n| dx \leq |A||\Omega|$. Hence, $\|v^n\|_{\mathrm{BV}(\Omega)}$ is uniformly bounded. So $\|e^{v^n}\|_{\mathrm{BV}(\Omega)}$ is uniformly bounded. The proof of v is the same as r, up to a subsequence also denoted by $\{v^n\}$ after relabeling, there exists a function $v^* \in \mathrm{BV}(\Omega)$ such that $v^n \to v^*$ a.e. $x \in \Omega$. Then, by the lower semi-continuity of the total variation and ℓ^2-norm, we also have

$$\begin{aligned} \|\nabla e^{v^*}\|_1 &\leq \liminf_{n\to\infty} \|\nabla e^{v^n}\|_1; \\ \|I - e^{v^*}\|_2^2 &\leq \liminf_{n\to\infty} \|I - e^{v^n}\|_2^2. \end{aligned} \tag{13}$$

Finally, since $r^n \to r^*$ a.e. $x \in \Omega$, $l^n \to l^*$ a.e. $x \in \Omega$, $v^n \to v^*$ a.e. $x \in \Omega$, Fatou's lemma gives that

$$\|v^* - r^* - l^*\|_2^2 \leq \liminf_{n\to\infty} \|v^n - r^n - l^n\|_2^2. \tag{14}$$

Combining inequalities from (11) to (14), we deduce that

$$\mathcal{F}(v^*, r^*, l^*) \leq \liminf_{n\to\infty} \mathcal{F}(v^n, r^n, l^n) = \inf \mathcal{F}(v, r, l).$$

which indicates that (v^*, r^*, l^*) is a minimizer of problem (9). This completes the proof. □

4. **The alternating minimization algorithm.** In this section, we discuss the minimization of (9). Since the variables v, r and l are coupled together, an accurate joint minimization can be costly. Thus, we use the alternating minimization algorithm to solve the minimization problem (9), through which one can obtain the minimizer approximately [32, 33, 34]; see Algorithm I.

Algorithm I: Alternating minimization algorithm for (9)

---

1. Initialization: choose $v^0 = r^0 = log(I)$ and select the parameters α, β, γ, μ, τ;
2. Iterations:

$$\begin{cases} v^{n+1} = \underset{v}{\operatorname{argmin}} \ \frac{1}{2}\|I - e^v\|_2^2 + \alpha\|\nabla e^v\|_1 + \frac{\mu}{2}\|v - r^n - l^n\|_2^2; & (15) \\ r^{n+1} = \underset{r}{\operatorname{argmin}} \ \beta\|\nabla r\|_1 + \frac{\mu}{2}\|v^{n+1} - r - l^n\|_2^2; & (16) \\ l^{n+1} = \underset{l}{\operatorname{argmin}} \ \gamma\|\nabla^2 l\|_1 + \frac{\mu}{2}\|v^{n+1} - r^{n+1} - l\|_2^2 + \frac{\tau}{2}\|l\|_2^2; & (17) \end{cases}$$

3. End till the stopping criterion meets:

$$\max(R(r^n, l^n)) \leq 10^{-5} \text{ or } n \geq 5 \times 10^3,$$

where the $R(r^n, l^n)$ is defined in section 5.

4.1. **Sub-minimization problem with respect to v.** In (15), the gradient and exponential function are coupled together, which increases the difficulty of computation. Therefore, we introduce a new variable $u = e^v$, and reformulate the minimization problem (15) as the following constrained minimization problem

$$\begin{aligned} \min_{v,u} \quad & \frac{1}{2}\|I - u\|_2^2 + \alpha\|\nabla u\|_1 + \frac{\mu}{2}\|v - r - l\|_2^2, \\ \text{s.t.,} \quad & u = e^v. \end{aligned} \tag{18}$$

We are going to minimize the variable u, which belongs to the category of ℓ^1-regularized problems with the general form as follows

$$\min_u \ \|\Phi(u)\|_1 + H(u), \tag{19}$$

where both $\|\Phi(u)\|_1$ and $H(u)$ are convex functions. The key idea to efficiently solve the minimization problem (19) is to split the two portions in (19) as [33, 34]. For our case, rather than considering (18), we introduce another auxiliary variable $\boldsymbol{p}$ and consider the following constrained optimization problem

$$\begin{aligned} \min_{v,u,\boldsymbol{p}} \quad & \frac{1}{2}\|I - u\|_2^2 + \alpha\|\boldsymbol{p}\|_1 + \frac{\mu}{2}\|v - r - l\|_2^2, \\ \text{s.t.,} \quad & u = e^v, \quad \boldsymbol{p} = \nabla u. \end{aligned} \tag{20}$$

Based on the augmented Lagrangian method, we can obtain the equivalent unconstrained optimization problem as

$$\begin{aligned}\max_{\Lambda_1,\boldsymbol{\Lambda_2}}\min_{v,u,\boldsymbol{p}}\mathcal{L}(v,u,\boldsymbol{p};\Lambda_1,\boldsymbol{\Lambda_2}) := \frac{1}{2}\|I-u\|_2^2+\alpha\|\boldsymbol{p}\|_1+\frac{\mu}{2}\|v-r-l\|_2^2+\langle\Lambda_1,u-e^v\rangle\\ +\frac{r_1}{2}\|u-e^v\|_2^2+\langle\boldsymbol{\Lambda_2},\boldsymbol{p}-\nabla u\rangle+\frac{r_2}{2}\|\boldsymbol{p}-\nabla u\|_2^2,\end{aligned} \tag{21}$$

where Λ_1 and $\boldsymbol{\Lambda_2}$ are Lagrange multipliers, and r_1, r_2 are positive penalty parameters. It is straightforward to separate (21) into the following three subproblems

$$\begin{cases} v^{n+1}=\underset{v}{\operatorname{argmin}}\ \langle\Lambda_1^n,-e^v\rangle+\frac{r_1}{2}\|u^n-e^v\|_2^2+\frac{\mu}{2}\|v-r^n-l^n\|_2^2; & (22)\\ u^{n+1}=\underset{u}{\operatorname{argmin}}\ \frac{1}{2}\|I-u\|_2^2+\frac{r_1}{2}\|u-(e^{v^{n+1}}-\frac{\Lambda_1^n}{r_1})\|_2^2+\frac{r_2}{2}\|\nabla u-(\boldsymbol{p}^n+\frac{\boldsymbol{\Lambda_2^n}}{r_2})\|_2^2; & (23)\\ \boldsymbol{p}^{n+1}=\underset{\boldsymbol{p}}{\operatorname{argmin}}\ \alpha\|\boldsymbol{p}\|_1+\langle\boldsymbol{\Lambda_2^n},\boldsymbol{p}\rangle+\frac{r_2}{2}\|\boldsymbol{p}-\nabla u^{n+1}\|_2^2. & (24)\end{cases}$$

The subproblems (22), (23) and (24) can be efficiently solved based on closed-form solutions. For (22), its Euler-Lagrange equation gives a nonlinear equation due to the exponential function of v. Let $g(v)=\langle\Lambda_1^n,-e^v\rangle+\frac{r_1}{2}\|u^n-e^v\|_2^2$, which is linearized by its Taylor expansion as follows [35]

$$g(v)\approx\langle\Lambda_1^n,-e^{v^n}\rangle+\frac{r_1}{2}\|e^{v^n}-u^n\|_2^2+\Big\langle\langle\Lambda_1^n,-e^{v^n}\rangle+r_1\langle e^{v^n}-u^n,e^{v^n}\rangle,v-v^n\Big\rangle.$$

By adding an extra proximal term [36] and deleting the constant terms, we arrive at the following minimization problem for v

$$\min_v\ \Big\langle r_1\langle e^{v^n}-u^n,e^{v^n}\rangle-\Lambda_1^n e^{v^n},v\Big\rangle+\frac{1}{2}\|v-v^n\|_2^2+\frac{\mu}{2}\|v-r^n-l^n\|_2^2,$$

the solution of which gives us

$$v^{n+1}=\frac{\Lambda_1^n e^{v^n}-r_1e^{v^n}(e^{v^n}-u^n)+v^n+\mu(r^n+l^n)}{1+\mu}. \tag{25}$$

For (23), its optimality condition gives us the following linear equation

$$\big((1+r_1)\mathcal{I}-r_2\Delta\big)u=I+r_1e^{v^{n+1}}-\Lambda_1^n-r_2\mathrm{div}\boldsymbol{p}^n-\mathrm{div}\boldsymbol{\Lambda_2^n}, \tag{26}$$

where $\mathcal{I}$ is the identity operator. By the periodic boundary condition for u, (26) becomes a block circulant system, which can be efficiently solved by the fast Fourier transform (FFT). Denoting $\mathcal{F}(u)$ as its Fourier transform, we can express the solution to u as follows:

$$u^{n+1}=\mathcal{F}^{-1}\left(\frac{\mathcal{F}(I+r_1e^{v^{n+1}}-\Lambda_1^n)-\mathcal{F}(\mathring{D}_x^-)\mathcal{F}(r_2p^{n,1}+\Lambda_2^{n,1})-\mathcal{F}(\mathring{D}_y^-)\mathcal{F}(r_2p^{n,2}+\Lambda_2^{n,2})}{(1+r_1)\mathcal{I}-r_2\big(\mathcal{F}(\mathring{D}_x^-)\mathcal{F}(\mathring{D}_x^+)+\mathcal{F}(\mathring{D}_y^-)\mathcal{F}(\mathring{D}_y^+)\big)}\right), \tag{27}$$

where $\boldsymbol{p}^n=(p^{n,1},p^{n,2})$, $\boldsymbol{\Lambda_2^n}=(\Lambda_2^{n,1},\Lambda_2^{n,2})$.

For (24), we can efficiently solve it using the shrinkage operator as follows

$$\boldsymbol{p}^{n+1}=\mathrm{shrink}(\nabla u^{n+1}-\frac{\boldsymbol{\Lambda_2^n}}{r_2},\frac{\alpha}{r_2}), \tag{28}$$

where $\mathrm{shrink}(\omega,\lambda)=\frac{\omega}{\|\omega\|_1}*\max(\|\omega\|_1-\lambda,0)$.

Besides, we update the Lagrange multipliers Λ_1 and $\boldsymbol{\Lambda_2}$ according to their gradient ascent direction as

$$\begin{cases}\Lambda_1^{n+1}=\Lambda_1^n+r_1(u^{n+1}-e^{v^{n+1}});\\ \boldsymbol{\Lambda_2^{n+1}}=\boldsymbol{\Lambda_2^n}+r_2(\boldsymbol{p}^{n+1}-\nabla u^{n+1}).\end{cases}$$

4.2. **Sub-minimization problems with respect to r and l.** As observed, both the sub-minimization problems with respect to r and l are ℓ^1 regularized optimization problems. Therefore, we can discuss the solutions to (16) and (17) together. Similar to the subproblem of u, we separate the ℓ^1 term and ℓ^2 term by introducing new variables $\boldsymbol{x} = \nabla r$ and $\boldsymbol{y} = \nabla^2 l$, and solve the corresponding constrained optimization problems based on the augmented Lagrangian method. Here, we omit the implementation details and provide the updating scheme to all variables as follows

$$\begin{cases} r^{n+1} = \underset{r}{\operatorname{argmin}} \ \frac{\mu}{2}\|v^{n+1} - r - l^n\|_2^2 - \langle \boldsymbol{\Lambda_3^n}, \nabla r\rangle + \frac{r_3}{2}\|\boldsymbol{x}^n - \nabla r\|_2^2; & (29) \\ \boldsymbol{x}^{n+1} = \underset{\boldsymbol{x}}{\operatorname{argmin}} \ \beta\|\boldsymbol{x}\|_1 + \langle \boldsymbol{\Lambda_3^n}, \boldsymbol{x}\rangle + \frac{r_3}{2}\|\boldsymbol{x} - \nabla r^{n+1}\|_2^2; & (30) \\ l^{n+1} = \underset{l}{\operatorname{argmin}} \ \frac{\mu}{2}\|v^{n+1} - r^{n+1} - l\|_2^2 - \langle \boldsymbol{\Lambda_4^n}, \nabla^2 l\rangle + \frac{r_4}{2}\|\boldsymbol{y}^n - \nabla^2 l\|_2^2 + \frac{\tau}{2}\|l\|_2^2; & (31) \\ \boldsymbol{y}^{n+1} = \underset{\boldsymbol{y}}{\operatorname{argmin}} \ \gamma\|\boldsymbol{y}\|_1 + \langle \boldsymbol{\Lambda_4^n}, \boldsymbol{y}\rangle + \frac{r_4}{2}\|\boldsymbol{y} - \nabla^2 l^{n+1}\|_2^2; & (32) \end{cases}$$

where $\boldsymbol{\Lambda_3}$ and $\boldsymbol{\Lambda_4}$ are Lagrange multipliers, and r_3, r_4 are penalty parameters.

For the subproblem (29) and (31), we can solve them using the FFT under the periodic boundary conditions. For the subproblem (30) and (32), there are the closed-form solutions based on the shrinkage operators. In addition, we update the Lagrange multipliers as follows

$$\begin{cases} \boldsymbol{\Lambda_3^{n+1}} = \boldsymbol{\Lambda_3^n} + r_3(\boldsymbol{x}^{n+1} - \nabla r^{n+1}); \\ \boldsymbol{\Lambda_4^{n+1}} = \boldsymbol{\Lambda_4^n} + r_4(\boldsymbol{y}^{n+1} - \nabla^2 l^{n+1}). \end{cases}$$

5. Numerical experiments.

In this section, we conduct a series of experiments on synthetic images with different illusions and noises of different distributions to demonstrate the performance of the proposed method.

5.1. **Tests of gaussian noises.** There are several parameters in our model (9), i.e., the regularization parameters α, β, γ, the penalty parameter μ and the theoretical parameter τ. The regularization parameter α and β are most critical parameters in our model. In the numerical tests, we choose α from $\alpha = 0.001$ to $\alpha = 0.1$ according to the severity of noises while choose β from $\beta = 0.001$ to $\beta = 0.05$ depending on the illusion. For different test images, the parameters γ, μ, τ are fixed as $\gamma = 0.08$, $\mu = 0.7$ and $\tau = 1e-5$. All other penalty parameters are set to $r_i = 0.2$, for $i = 1, 2, 3, 4$.

Three other variational methods, including TVH1 model [19], HoTVL1 model [25] and L0MS model [24], are evaluated and compared with our model. We list the implementation details of each algorithm as follows

① TVH1: the model is sensitive to the parameter of the regularization term on reflectance. We adjust β from $\beta = 0.1$ to $\beta = 25$, and fix $\alpha = 0.1$, $\tau = 1e-5$ for different examples.

② HoTVL1: the model is sensitive to the parameter of the regularization term on reflectance. We tune α from $\alpha = 0.01$ to $\alpha = 0.1$, and set $\beta = 10$, $\tau = 1e-5$. The box constraints are fixed as $\mathcal{B}_r = [-20, 0]$ and $\mathcal{B}_l = [-20, 0]$ for the best performance.

③ L0MS: the model is sensitive to the parameter of the regularization term on reflectance. We choose α from $\alpha = 0.01$ to $\alpha = 0.1$, and fix $\beta = 1$, $\tau = 1e-5$.

5.1.1. ***Stable performance for noises.*** In magnetic resonance imaging (MRI), the reconstructed images are often corrupted by the bias field due to the inhomogeneous illuminations. We use two slices of T_1-weighted brain MR image as examples, which are contaminated by 3%, 5%, 7%, 9% noise and 40% intensity non-uniformity (downloaded from McGill BrainWeb: http://www. bic.mni.mcgill.ca/brainweb/). Both the recovered results and zoomed details of TVH1 model, HoTVL1 model, L0MS model and our model are displayed in FIGURE 1. It can be seen that all comparable methods are sensitive to noises, while the proposed model can well remove the noises and the intensity inhomogeneity simultaneously. On the other hand, we compute the Peak Signal to Noise Ratio (PSNR) and Mean Structural Similarity (MSSIM) to quantitatively evaluate the results, which are listed the results in TABLE 1. As observed both PSNR and MSSIM are in accordance with the visual results, that better values are always achieved by the proposed model. Since our model uses the same regularization terms for reflectance and illusion as HoTVL1, high PSNR and MSSIM are mainly due to the effective control of the noises. Note that we are using ETV to represent our model in FIGURE and TABLE.

		3%		5%		7%		9%	
		PSNR	MSSIM	PSNR	MSSIM	PSNR	MSSIM	PSNR	MSSIM
Test Image1	TVH1	26.8369	0.9436	25.2879	0.9174	24.4622	0.8933	23.2509	0.8629
	HoTVL1	29.7605	0.9515	27.4964	0.9342	26.6143	0.9214	25.2707	0.9063
	L0MS	29.6193	0.9198	27.4895	0.9033	26.1466	0.8915	24.3937	0.8650
	ETV	**32.6749**	**0.9904**	**31.1170**	**0.9844**	**29.1291**	**0.9767**	**28.4244**	**0.9686**
Test Image2	TVH1	27.3897	0.9229	26.4466	0.8932	25.4457	0.8655	23.7962	0.8334
	HoTVL1	29.5698	0.9321	28.7948	0.9142	27.1248	0.8988	25.4362	0.8833
	L0MS	31.8155	0.9227	28.5140	0.8950	27.1074	0.8746	24.8900	0.8374
	ETV	**33.4328**	**0.9911**	**31.4092**	**0.9842**	**29.8200**	**0.9764**	**28.6543**	**0.9698**

TABLE 1. PSNR and MSSIM of T_1-weighted brain MR images with different levels of noises.

For this example, we set $\beta \in [10, 24]$ for TVH1 model, $\alpha \in [0.02, 0.05]$, $\tau = 1e-3$ for HoTVL1 model and $\alpha \in [0.04, 0.07]$ for L0MS model according to the noise levels. For our model, we choose $\alpha \in [0.01, 0.04]$ and fix $\beta = 0.002$.

5.1.2. ***Stable performance for intensity inhomogeneities.*** We select one slice from the T_1-weighted brain volume and generate 10 images by adding Gaussian white noise of mean 0 and variance 0.001 and intensity inhomogeneities of different profiles. We plot the PSNR and MSSIM obtained from the four methods in FIGURE 2, which illustrates that our model gives the best denoising results. Indeed, our model is shown stable with respect to different profiles of intensity inhomogeneities. Moreover, we present two of the 10 examples and the corresponding results in FIGURE 3. The ground truth and the estimated bias field of the proposed model are given in FIGURE 4. Despite the great difference of the bias field, the proposed method can correctly estimate its distribution. As shown in FIGURE 4 (c), the improvement of the image quality is further demonstrated by the histograms, where four well-defined peaks can be observed in the histograms of the bias corrected image corresponding to the background, Cerebrospinal Fluid (CSF), Gray Matter (GM) and White Matter (WM). In contrast, the histograms of the original images do not present such well-separated peaks due to the existence of the bias field.

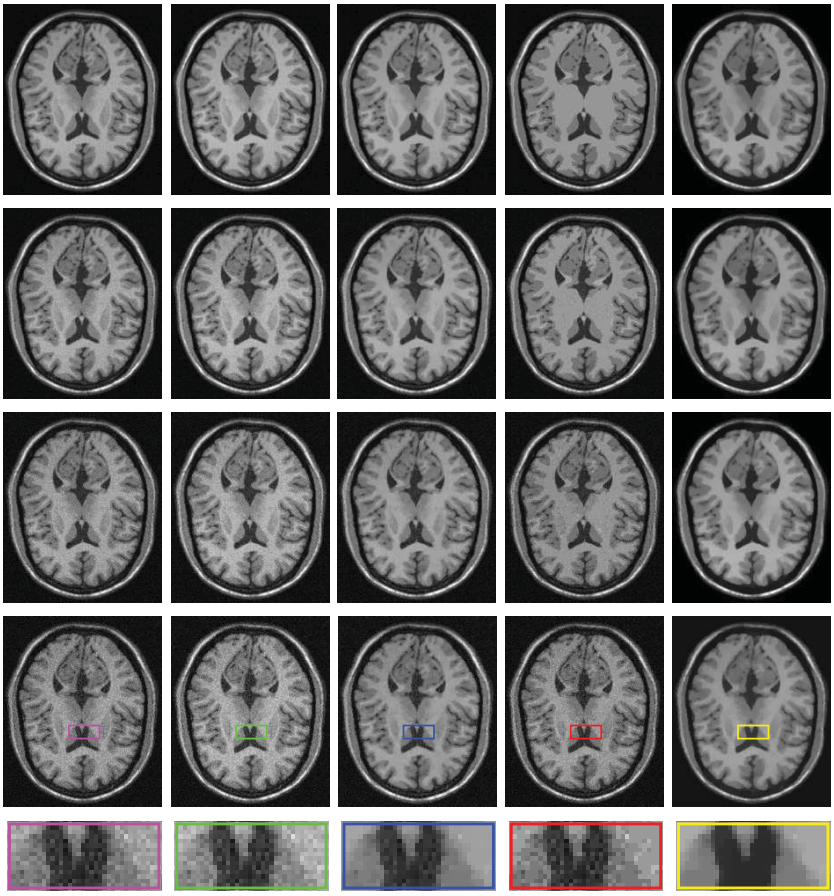

(a) Input (b) TVH1(R) (c) HoTVL1(R) (d) L0MS(R) (e) ETV(R)

FIGURE 1. Performances of four methods on T_1-weighted brain MR images with different levels of noises.

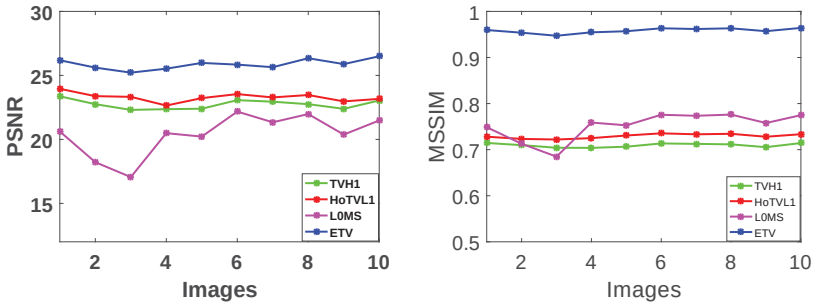

FIGURE 2. Comparison among the four methods in terms of PSNR and MSSIM for images with different intensity inhomogeneities.

On the other hand, we evaluate the performance of bias correction using the coefficient of variations (CV), which is defined for each tissue T as

$$\mathrm{CV(T)} = \frac{\sigma(\mathrm{T})}{\mu(\mathrm{T})} \times 100\%,$$

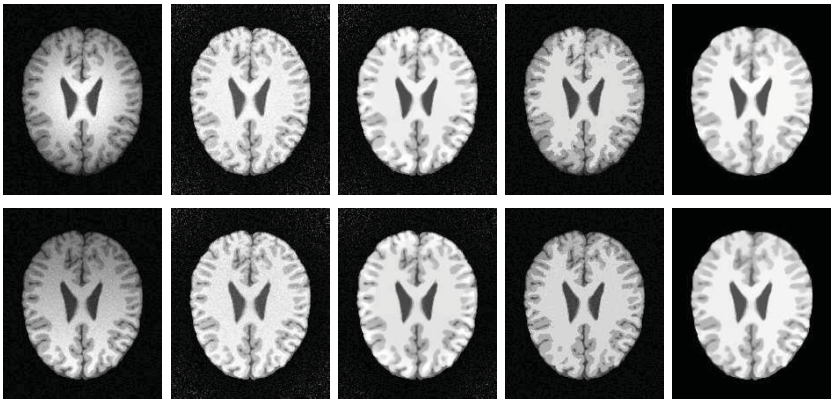

(a) Input (b) TVH1(R) (c) HoTVL1(R) (d) L0MS(R) (e) ETV(R)

FIGURE 3. Performances of four methods on T_1-weighted brain images with different intensity inhomogeneities.

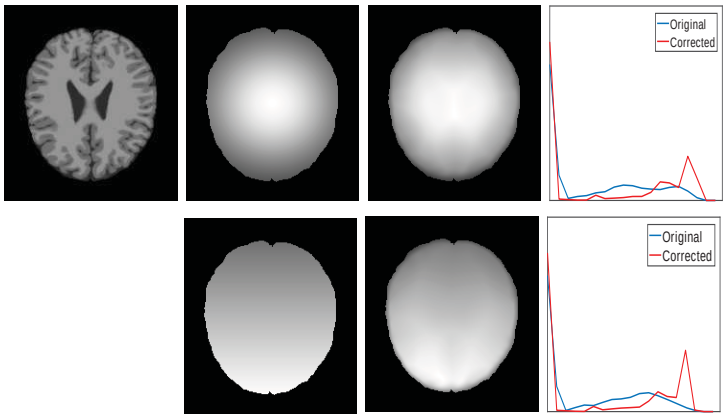

(a) Truth L (b) Estimated L (c) Histogram

FIGURE 4. Ground truth and estimated bias field of the proposed method with examples in FIGURE 3.

where $\sigma(\mathrm{T})$ and $\mu(\mathrm{T})$ are the standard deviation and the mean of the intensities in the tissue T. The CV values of white matter, gray matter and cerebrospinal fluid are evaluated on the bias corrected images and plotted by the boxplots in FIGURE 5. We can see that the CV obtained by our model is significantly better than other methods, which demonstrate the advantages of the proposed model in dealing with noises and intensity inhomogeneities.

For this experiment, we set $\beta = 0.15$ for TVH1 model, $\alpha = 0.08$ for HoTVL1 model, and $\alpha = 0.06$ for L0MS model in order to achieve the best results. For our model, we fix $\alpha = 0.01$ and $\beta = 0.02$.

5.1.3. ***Convergence analysis.*** To check the convergence of the iteration process, we monitor the relative errors of the solution r^n and l^n, which are defined as

$$R(r^n, l^n) = \Big(\frac{\|r^n - r^{n-1}\|_2^2}{\|r^n\|_2^2}, \frac{\|l^n - l^{n-1}\|_2^2}{\|l^n\|_2^2} \Big).$$

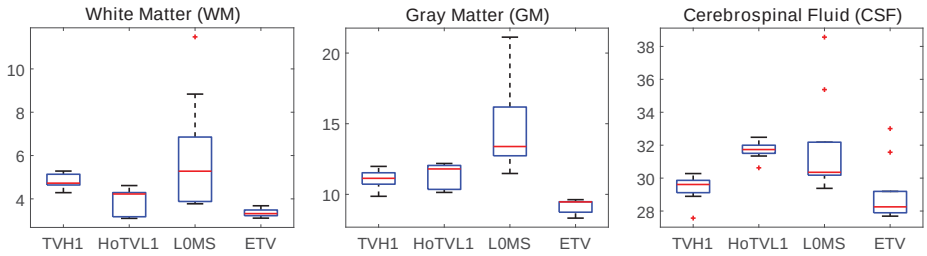

FIGURE 5. Comparison of the performance in terms of CV(%).

We use the first image in FIGURE 3 as an example, and plot the relative errors in FIGURE 6 (a) and (b). Besides, we also track the numerical energy of the objective function in FIGURE 6 (c). It is shown that both the relative errors of r, l and the numerical energy decay as the iteration increase, which demonstrate that our model converges well numerically.

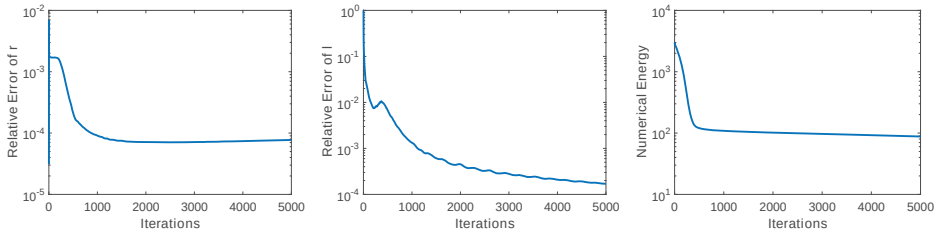

(a) (b) (c)

FIGURE 6. The relative errors of r and l and numerical energy of our model for the first image in FIGURE 3.

5.1.4. ***Applications on real data.*** In this experiment, we test the proposed model on the real MR images including an MR image of bladder and two MR images of brain, which are shown in FIGURE 7 (a). The results of R and L in FIGURE 7 (b) and (c) demonstrate that the proposed model can well recover the real intensities and enhance the quality of the images.

5.2. **Extension to color images.** The proposed model can be extended to shadowed color images as shown in FIGURE 8. We use the HSV (hue, saturation, value) color space and process in the Value (V) channel, which means both the shadow and noise contaminate the V channel. The results of HoTVL1 model and our model are exhibited in FIGURE 8 (b) and (c), respectively. It is obviously that the proposed model can remove the noises as well as the shadow effect.

For this example, the parameters used in HoTVL1 model are $\alpha = 0.15$ for Test image and $\alpha = 0.3$ for Wall image, other parameters are the same as the previous experiments. For our model, the parameters are $\beta = 0.002$, $\gamma = 0.004$ for Test image and $\beta = 0.045$, $\gamma = 0.08$ for Wall image. Other parameters are fixed as $\alpha = 0.05$, $\mu = 0.06$, $\tau = 1e-5$ and $r_i = 0.05$ for $i = 1, \cdots, 4$.

5.3. **Extension to impulsive noise.** One advantage of the proposed model (9) is its flexibility in dealing with different noises. The impulsive noise is often generated by malfunctioning pixels in camera sensors, faulty memory locations in hardware,

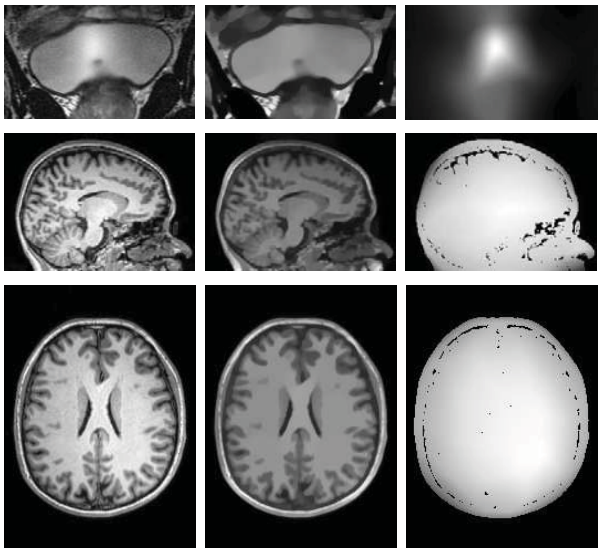

(a) Input (b) R (c) L

FIGURE 7. Tests on real MR images. The parameters used in our model are $\alpha = 0.03$ and $\beta = 0.015$.

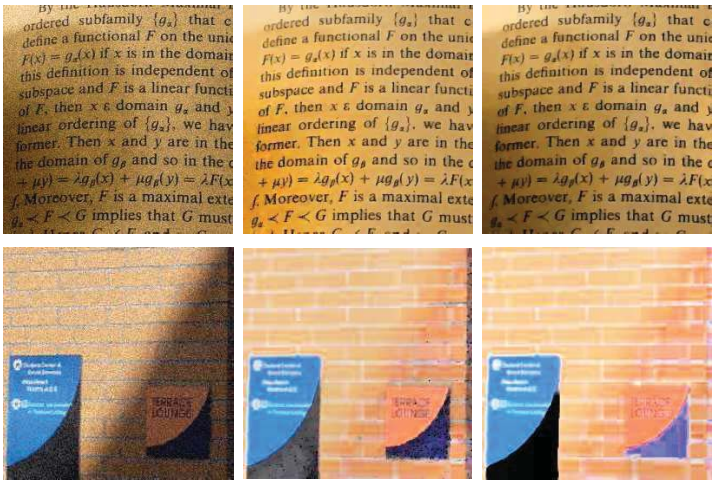

(a) Input (b) HoTVL1(R) (c) ETV(R)

FIGURE 8. Tests on color images of HoTVL1 model and our model.

or erroneous transmission [27]. Based on the Bayesian statistic, one can derive a ℓ^1 fidelity term, which can exactly fit uncorrupted pixels and perfectly regularize the corrupted pixels by the impulsive noise. Indeed, the ℓ^1 fidelity term only affects the sub-minimization problem w.r.t. v, which has the fast numerical solver [37]. In particular, we consider the following minimization problem for images corrupted by

salt-and-pepper noise:

$$\min_{v,r,l} \|I - e^v\|_1 + \alpha\|\nabla e^v\|_1 + \beta\|\nabla r\|_1 + \gamma\|\nabla^2 l\|_1 + \frac{\mu}{2}\|v - r - l\|_2^2 + \frac{\tau}{2}\|l\|_2^2. \quad (33)$$

We use the Adelson's checkerboard shadow image and the Logvinenko's cube shadow image as examples, which are two typical test images for Retinex illusion. We add the salt-and-pepper noise from 20% to 50% to both images. The reflectance component R and illumination component L obtained by the proposed method are displayed in FIGURE 9 and FIGURE 10. The visual results demonstrate that our model can well decompose the reflectance and illumination although the test images contain impulsive noises.

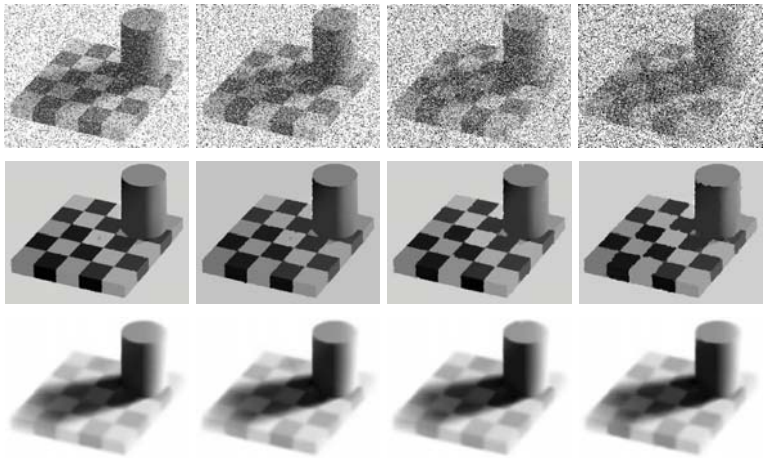

(a) 20% (b) 30% (c) 40% (d) 50%

FIGURE 9. Decomposition of the checkboard image.

For the impulsive noises, we fix $\beta = 0.05$, $\gamma = 0.08$, $\mu = 0.6$, $\tau = 1e-5$ and $r_i = 0.5$ for $i = 1, \cdots, 5$, while we select α according to the level of the noises from $\alpha = 0.6$ to $\alpha = 0.9$.

5.4. **Extension to Poisson noise.** The Poisson noise is another common seen noise, which may be contained in radiography, fluorescence microscopy and positron-emission-tomography images [28]. According to the the characteristic of Poisson distribution, the Kullback-Leibler (KL) divergence is used as the fidelity term. Therefore, we propose the following minimization problem for images containing Poisson noise:

$$\min_{v,r,l} \langle e^v - Iv, 1\rangle + \alpha\|\nabla e^v\|_1 + \beta\|\nabla r\|_1 + \gamma\|\nabla^2 l\|_1 + \frac{\mu}{2}\|v - r - l\|_2^2 + \frac{\tau}{2}\|l\|_2^2. \quad (34)$$

In FIGURE 11, we add Poisson noise into two synthetic images. Both R and L are presented in FIGURE 11, which show that the proposed model can obtain visually preferable results compared to the original ones.

For this experiment, we set $\alpha = 0.03$, $\beta = 0.015$, $\gamma = 0.08$, $\mu = 0.6$, $\tau = 1e-5$ and $r_i = 0.5$ for $i = 1, \cdots, 5$.

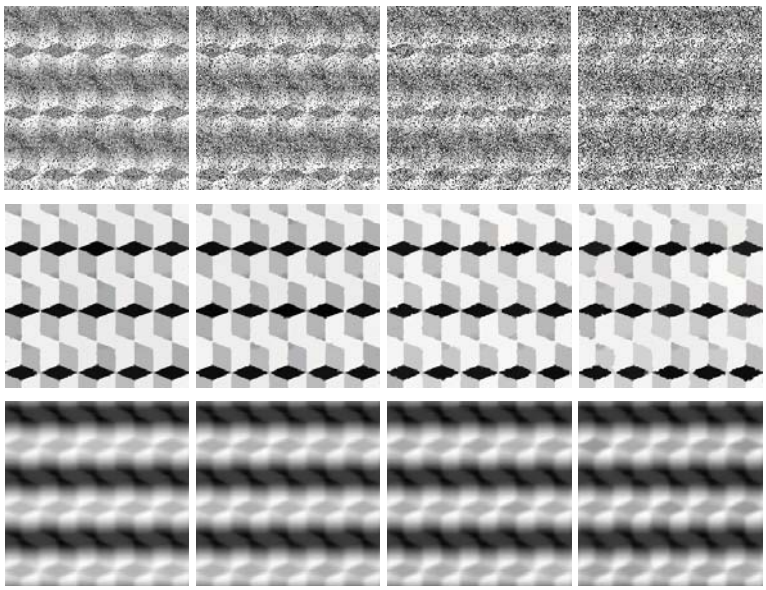

(a) 20% (b) 30% (c) 40% (d) 50%

FIGURE 10. Decomposition of the logvi image.

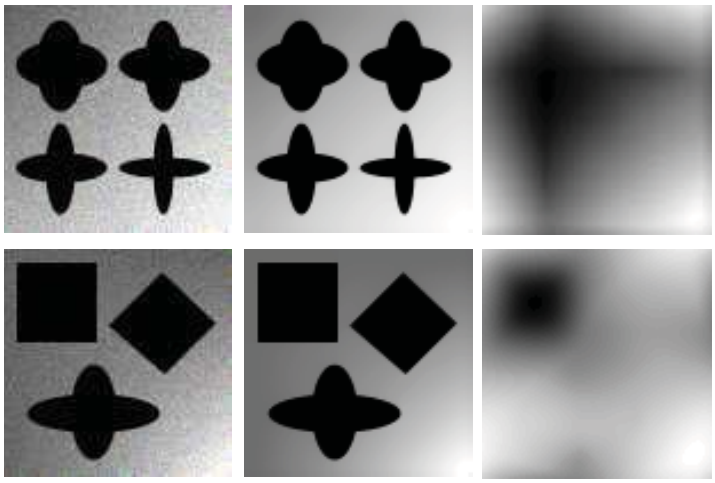

(a) Input (b) R (c) L

FIGURE 11. Denoising and decomposition of the images containing Poisson noise.

6. **Conclusion and future works.** In this paper, we have presented an efficient variational model for Retinex, which was developed based on a new image model by decomposing a given image into reflectance, illumination and noises. The proposed model was shown coercive, which guarantee the existence of the minimizers. We designed an efficient alternating minimization algorithm, where all subproblems can be solved by the closed-form solutions. The framework is easy to be adopted to other Retinex models and robust with noises of different modalities. Various

numerical results were implemented to demonstrate the advantages of our model over the existing method for Retinex applications. In the future, we may consider to extend the proposed model to the multiplicative noises, and discuss the convexity and the global convergence of the proposed model.

REFERENCES

[1] L. I. Rudin, S. Osher and E. Fatemi, Nonlinear total variation based noise removal algorithms, *Physica D: Nonlinear Phenomena*, **60(1-4)** (1992), 259–268.

[2] A. Chambolle and P.-L. Lions, Image recovery via total variation minimization and related problems, *Numerische Mathematik*, **76(2)** (1997), 167–188.

[3] J.-F. Aujol and A. Chambolle, Dual norms and image decomposition models, *International Journal of Computer Vision*, **63(1)** (2005), 85–104.

[4] J.-F. Aujol, G. Gilboa, T. Chan and S. Osher, Structure-texture image decomposition–modeling, algorithms, and parameter selection, *International Journal of Computer Vision*, **67(1)** (2006), 111–136.

[5] E. H. Land and J. J. McCann, Lightness and retinex theory, *Journal of the Optical Society of America*, **61(1)** (1971), 1–11.

[6] E. H. Land, Recent advances in retinex theory and some implications for cortical computations: color vision and the natural image, *Proceedings of the National Academy of Sciences*, **80(16)** (1983), 5163–5169.

[7] T. J. Cooper and F. A. Baqai, Analysis and extensions of the frankle-mccann retinex algorithm, *Journal of Electronic Imaging*, **13(1)** (2004), 85–93.

[8] E. Provenzi, D. Marini, L. De Carli and A. Rizzi, Mathematical definition and analysis of the retinex algorithm, *Journal of the Optical Society of America A*, **22(12)** (2005), 2613–2621.

[9] E. H. Land, An alternative technique for the computation of the designator in the retinex theory of color vision, *Proceedings of the National Academy of Sciences*, **83(10)** (1986), 3078–3080.

[10] J. McCann, Lessons learned from mondrians applied to real images and color gamuts, in *Proceedings of the IST/SID 7th Color Imaging Conference*, (1999), 1–8.

[11] O. Faugeras, Digital color image processing within the framework of a human visual model, *IEEE Transactions on Acoustics, Speech, and Signal Processing*, **27(4)** (1979), 380–393.

[12] D. J. Jobson, Z.-u. Rahman and G. A. Woodell, Properties and performance of a center/surround retinex, *IEEE Transactions on Image Processing*, **6(3)** (1997), 451–462.

[13] M. Bertalmío, V. Caselles and E. Provenzi, Issues about retinex theory and contrast enhancement, *International Journal of Computer Vision*, **83(1)** (2009), 101–119.

[14] M. Bertalmío, V. Caselles, E. Provenzi and A. Rizzi, Perceptual color correction through variational techniques, *IEEE Transactions on Image Processing*, **16(4)** (2007), 1058–1072.

[15] R. Palma-Amestoy, E. Provenzi, M. Bertalmío and V. Caselles, A perceptually inspired variational framework for color enhancement, *IEEE Transactions on Pattern Analysis and Machine Intelligence*, **31(3)** (2009), 458–474.

[16] J. M. Morel, A. B. Petro and C. Sbert, A pde formalization of retinex theory, *IEEE Transactions on Image Processing*, **19(11)** (2010), 2825–2837.

[17] R. Kimmel, M. Elad, D. Shaked, R. Keshet and I. Sobel, A variational framework for retinex, *International Journal of Computer Vision*, **52(1)** (2003), 7–23.

[18] M. Elad, Retinex by two bilateral filters, in *International Conference on Scale-Space Theories in Computer Vision*, Springer, Berlin, (2005), 217–229.

[19] M. K. Ng and W. Wang, A total variation model for retinex, *SIAM Journal on Imaging Sciences*, **4(1)** (2011), 345–365.

[20] W. Ma and S. Osher, A tv bregman iterative model of retinex theory, *Inverse Problems and Imaging*, **6(4)** (2012), 697–708.

[21] D. Zosso, G. Tran and S. Osher, Non-local retinex—a unifying framework and beyond, *SIAM Journal on Imaging Sciences*, **8(2)** (2015), 787–826.

[22] H. Chang, M. K. Ng, W. Wang and T. Zeng, Retinex image enhancement via a learned dictionary, *Optical Engineering*, **54(1)** (2015), 013107.

[23] Y. Duan, H. Chang, W. Huang and J. Zhou, Simultaneous bias correction and image segmentation via L_0 regularized mumford-shah model, in *2014 IEEE International Conference on Image Processing (ICIP)*, (2014), 6–10.

[24] Y. Duan, H. Chang, W. Huang, J. Zhou, Z. Lu and C. Wu, The L_0 regularized mumford-shah model for bias correction and segmentation of medical images, *IEEE Transactions on Image Processing*, **24(11)** (2015), 3927–3938.
[25] J. Liang and X. Zhang, Retinex by higher order total variation L^1 decomposition, *Journal of Mathematical Imaging and Vision*, **52(3)**(2015), 345–355.
[26] L. Liu, Z.-F. Pang and Y. Duan, A novel variational model for retinex in presence of severe noises, in *2017 IEEE International Conference on Image Processing (ICIP)*, (2017), 3490–3494.
[27] A. Bovik, *Handbook of Image and Video Processing*, Academic Press, 2000.
[28] T. Le, R. Chartrand and T. J. Asaki, A variational approach to reconstructing images corrupted by poisson noise, *Journal of Mathematical Imaging and Vision*, **27(3)** (2007), 257–263.
[29] H. Chang, W. Huang, C. Wu, S. Huang, C. Guan, S. Sekar, K. K. Bhakoo and Y. Duan, A new variational method for bias correction and its applications to rodent brain extraction, *IEEE Transactions on Medical Imaging*, **36(3)** (2017), 721–733.
[30] Y.-M. Huang, M. K. Ng and Y.-W. Wen, A new total variation method for multiplicative noise removal, *SIAM Journal on Imaging Sciences*, **2(1)** (2009), 20–40.
[31] K. Papafitsoros and C.-B. Schönlieb, A combined first and second order variational approach for image reconstruction, *Journal of Mathematical Imaging and Vision*, **48(2)** (2014), 308–338.
[32] Y. Wang, J. Yang, W. Yin and Y. Zhang, A new alternating minimization algorithm for total variation image reconstruction, *SIAM Journal on Imaging Sciences*, **1(3)** (2008), 248–272.
[33] T. Goldstein and S. Osher, The split bregman method for L1-regularized problems, *SIAM Journal on Imaging Sciences*, **2(2)** (2009), 323–343.
[34] C. Wu and X.-C. Tai, Augmented lagrangian method, dual methods, and split bregman iteration for rof, vectorial tv, and high order models, *SIAM Journal on Imaging Sciences*, **3(3)** (2010), 300–339.
[35] M. Benning, F. Knoll, C.-B. Schönlieb and T. Valkonen, Preconditioned admm with nonlinear operator constraint, in *IFIP Conference on System Modeling and Optimization*, (2015), 117–126.
[36] X. Zhang, M. Burger and S. Osher, A unified primal-dual algorithm framework based on bregman iteration, *Journal of Scientific Computing*, **46(1)** (2011), 20–46.
[37] C. Wu, J. Zhang and X.-C. Tai, Augmented lagrangian method for total variation restoration with non-quadratic fidelity, *Inverse Problems and Imaging*, **5(1)** (2011), 237–261.

Received August 2017; revised March 2018.

E-mail address: liulu2015@tju.edu.cn
E-mail address: zhifengpang@163.com
E-mail address: yuping.duan@tju.edu.cn